Efficient PFAS Removal Using Reusable and Non-Toxic 3D Printed Porous Trianglamine Hydrogels

Arnaud Chaix, Chaimaa Gomri, Belkacem Tarek Benkhaled, Michel Habib, Romain Dupuis, Eddy Petit, Jason Richard, Antonin Segala, Laure Lichon, Christophe Nguyen, et al.

ADVANCED MATERIALS
www.advmat.de

Efficient PFAS Removal Using Reusable and Non-Toxic 3D Printed Porous Trianglamine Hydrogels

Arnaud Chaix, Chaimaa Gomri, Belkacem Tarek Benkhaled, Michel Habib, Romain Dupuis, Eddy Petit, Jason Richard, Antonin Segala, Laure Lichon, Christophe Nguyen, Magali Gary-Bobo, Sébastien Blanquer, and Mona Semsarilar**

Per- and polyfluoroalkyl substances (PFAS) are now a paramount concern in water remediation. Nowadays, urgent action is required for the development of advanced technologies aimed at capturing PFAS and mitigating their impact. To offer a solution, a functional 3D printed hydrogel tailored is designed to trap a broad spectrum of PFAS contaminants. The hydrogel is made of a photo-crosslinked dimethacrylate-ureido-trianglamine (DMU-Δ) and Pluronic P123 dimethacrylate (PDM) fabricated by stereolithography (SLA). With the aid of 3D-printing, porous and nonporous hydrogels (3D-PSHΔ, 3D-SHΔ) as well as quaternized hydrogels (3D-PSHΔQ^+) are prepared. These tailored hydrogels, show high uptake capacities and fast removal kinetics for PFAS from aqueous sources. The PFAS removal efficiency of these hydrogels are then compared to P123 hydrogels with no trianglamine (3D-SH). The 3D-SH hydrogel shows no affinity to PFAS, proving that the sorption is due to the interaction between the trianglamine (Δ) and PFAS. Metadynamic simulations also confirmed this interaction. The porous matrices showed the fastest and highest uptake capacity. 3D-PSHΔ is able to capture ≈ 91% of PFAS within 5 h using initial concentrations of 5 and 0.5 ppm in both deionized and river water. The sorption of PFAS is further enhanced by introducing permanent positive charges to the structure of the porous hydrogels, resulting in even faster sorption kinetics for both long and short PFAS chains with diverse polar heads. Besides the remarkable efficiency in capturing PFAS, these designed hydrogels are non-toxic and have outstanding chemical and thermal stability, making them a brilliant candidate for mass use in the combat against PFAS pollution.

1. Introduction

The extensive global contamination of water bodies with per- and polyfluoroalkyl substances (PFAS) is an escalating issue.[1] PFAS are organofluorine material, frequently dubbed as the "forever chemicals", since they are stable and not very easy to degrade.[2,3] For several decades, PFAS have been extensively used in diverse domains ranging from military, aerospace, electronics, construction, and automotive industries as well as in the production of consumer goods like cosmetics, textiles, packaging, non-stick cookware, oils, and inks.[2] This mass of use has led to significant contamination of water bodies with the most commonly used PFAS; perfluorooctanoic acid (PFOA) and perfluorooctanesulfonic acid (PFOS).[4] PFAS has been detected all over Europe and USA as well as in Polar Regions,[5] and Mount Everest.[6–8] The U.S. Environmental Protection Agency (U.S. EPA) and the European Council have set several regulations regarding PFAS in drinking water (0.07 μg L^{-1} (USA) and 0.5 μg L^{-1} (EU)).[9–11] The exceptional environmental persistence of PFAS is primarily

A. Chaix, C. Gomri, B. T. Benkhaled, E. Petit, J. Richard, A. Segala, M. Semsarilar
Institut Européen des Membranes (IEM)
Univ Montpellier
CNRS
ENSCM
Montpellier 34090, France
E-mail: Mona.semsarilar@umontpellier.fr

The ORCID identification number(s) for the author(s) of this article can be found under https://doi.org/10.1002/adma.202410720

DOI: 10.1002/adma.202410720

M. Habib, S. Blanquer
Institut Charles Gerhardt de Montpellier (ICGM)
Univ Montpellier
CNRS
ENSCM
Montpellier 34090, France
E-mail: sebastien.blanquer@umontpellier.fr

R. Dupuis
Laboratoire de Mécanique et Génie Civil (LMGC)
Univ Montpellier
CNRS-UMR 5508, Montpellier 34090, France

L. Lichon, C. Nguyen, M. Gary-Bobo
Institut des Biomolécules Max Mousseron (IBMM)
Univ Montpellier
CNRS
ENSCM
Montpellier 34090, France

due to the high thermodynamic stability of C-F bonds, with a bond dissociation energy of up to 130 kcal mol^{-1}, which makes degradation a daunting task.[12] Hence, the sorption of PFAS is the most promising method to reduce the contamination. The challenge for an efficient sorption is to develop novel adsorbents capable of removing PFAS to exceptionally low residual concentrations (<10 ng L^{-1}).[13] Currently, activated carbon (AC) is used for removal of PFAS. However, AC has a slow uptake (require long contact time) and notably low affinity for short-chain PFAS.[13] In addition, their regeneration is partial even via energy-intensive thermal treatment that besides being expensive, produces high amounts of CO_2.[14] These shortcomings have motivated the development of a wide range of functional material including carbon nanotubes (CNT),[15] 2D material,[16,17] magnetite nanoparticles,[18] ion-exchange resins,[19] cellulose,[20] metal-organic frameworks (MOFs),[21,22] covalent organic frameworks (COFs),[23,24] and porous organic polymers (POPs)[25,26] for PFAS removal. All the above mentioned material are in the form of powder that brings about a significant hurdle for their industrial use. Material in powder form are difficult to handle and transport (sensitivity to pressure and dust, clogging, mass loss and moisture). Moreover, their regeneration is often through energy and time-consuming techniques such as centrifugation and filtration. Although, few polymer supports, such as polysulfide, have been used to fix the powdered activated carbon (PAC).[27]

A new class of designed material known as macrocycle-based polymers could offer solutions. In such structures it is possible to optimize the molecular architecture and the host-guest interactions. To date, a multitude of macrocycles have been designed such as cucurbiturils,[28,29] cyclen,[30] calixarenes,[31] pillararenes,[32] prismarenes,[33] and Schiff base macrocycles.[34] These functional molecules possess sorption sites and cavities that can be selective toward specific guests. However, majority of reported macrocycles are difficult and expensive to make (multi-step reaction and purification steps, low yields, etc.) which is a major drawback for their industrial use. In contrast, Schiff base macrocycles such as trianglamines (Δ) present an ideal choice due to their soft synthesis conditions. In the past decade, trianglamines have been applied for several applications, such as gas capture and separation,[35] sensor technology,[36] membrane development,[37] iodine removal,[38] host-guest chemistry[39–46] and more recently as highly selective artificial water channels.[47] In literature there are examples of using macrocycles for PFAS capture, including cyclodextrins,[10,25] calixarenes,[12] pillararenes,[48] and guanidinocalix[5]arene.[4] A series of crosslinked material containing macrocycles was reported that demonstrated high capacity for adsorbing PFAS from water and groundwater. However, most of these materials contain fluoride groups, that are considered PFAS and would serve as an additional source of contamination at the end of their use.[7,12,13,25]

A useful class of polymers for sorption application is hydrogels. Hydrogels are characterized as crosslinked polymers with remarkable water absorption capacity.[49–51] In addition, hydrogels can be made as 3D objects with controlled designs via 3D printing. 3D printing permits fabrication of structures with specific geometries and controlled porosity allowing optimization of their sorption capacity.[52] However, there are not many reports on use of 3D printed hydrogels for water decontamination. For example, 3D printed hydrogels containing cellulose nanocrystals[53] and chitosan-Pluronic F-127[54] have been used for removal of charged dyes and heavy metal ions. 3D extruded nanocomposite hydrogels derived from biopolymers combined with inorganic additives such as graphenes,[55] nanoclays,[56,57] or MOFs,[58] have also been used for the capture of dyes, pesticides and heavy metal ions. The achievable pore geometry, low resolution and reproducibility are the current challenges of 3D extrusion process. Among the diverse 3D printing techniques, photo-polymerization methods, specifically stereolithography (SLA) (from laser or Digital Light Processing DLP), stands out as a particularly suitable method for the facile and efficient fabrication of photo-crosslinked hydrogels. SLA offers high resolution and allows for the formation of versatile architectures, with good potential to be employed at industrial scale.

In this study, we report for the first time a 3D printed porous hydrogel containing trianglamine for selective removal of PFAS. This novel material free of fluorine shows high capacity for rapid uptake of PFAS even in complex media such as river water. Further, it shows a stunning selectivity toward a range of different types of PFAS (chain length and ionic group) that is retained even after cycles of sorption-desorption (≥ 90%). It also displays a remarkable thermal and chemical stability. For better understanding of the sorption mechanism metadynamic simulations were conducted demonstrating the importance of the hydrophobic and ionic interactions. To ensure the safety (non-toxicity) of this novel adsorbent for environmental uses, they were tested on zebrafish. The findings suggest that it has a promising future for being used as the adsorbent of choice at large scale for the removal of PFAS from different aqueous media.

2. Results and Discussion

2.1. Synthesis of Trianglamine (Δ), Dimethacrylate-Ureido-Δ (DMU-Δ), and the Hydrogels (3D-SH, 3D-SHΔ, 3D-PSHΔ)

Trianglamine (Δ) was prepared, following the procedure reported by Gawronski and co-workers (Figure S1, Supporting Information).[34,59] The obtained Δ powder was characterized using ^{1}H and ^{13}C NMR in $CDCl_3$, confirming the chemical structure (Figures S2 and S3, Supporting Information). Additionally, high-resolution mass spectrum (ESI-MS+) and elemental analysis were conducted. The results align well with the proposed formula, indicating a molecular weight of 649.5 $g.mol^{-1}$ (Figures S4 and S5, Supporting Information). Methacrylate arms were grafted on Δ using 2-Isocyanatoethyl methacrylate (IEM) (**Scheme 1a**). The high yield synthesis involved adding two equivalents of IEM, resulting in the formation of dimethacrylate-ureido-Δ (DMU-Δ) as the major product. The aim of adding two equivalences was to keep the maximum of free secondary amine groups for a better electrostatic interaction with PFAS molecules and also to keep the possibilities to chemically quaternized the Δ with iodomethane. DMU-Δ was characterized using ^{1}H, ^{13}C NMR, and high-resolution mass spectrum (ESI-MS+) (Figures S6–S8, Supporting Information). In parallel, P123 was end-functionalized with two methacrylate end-groups to act as

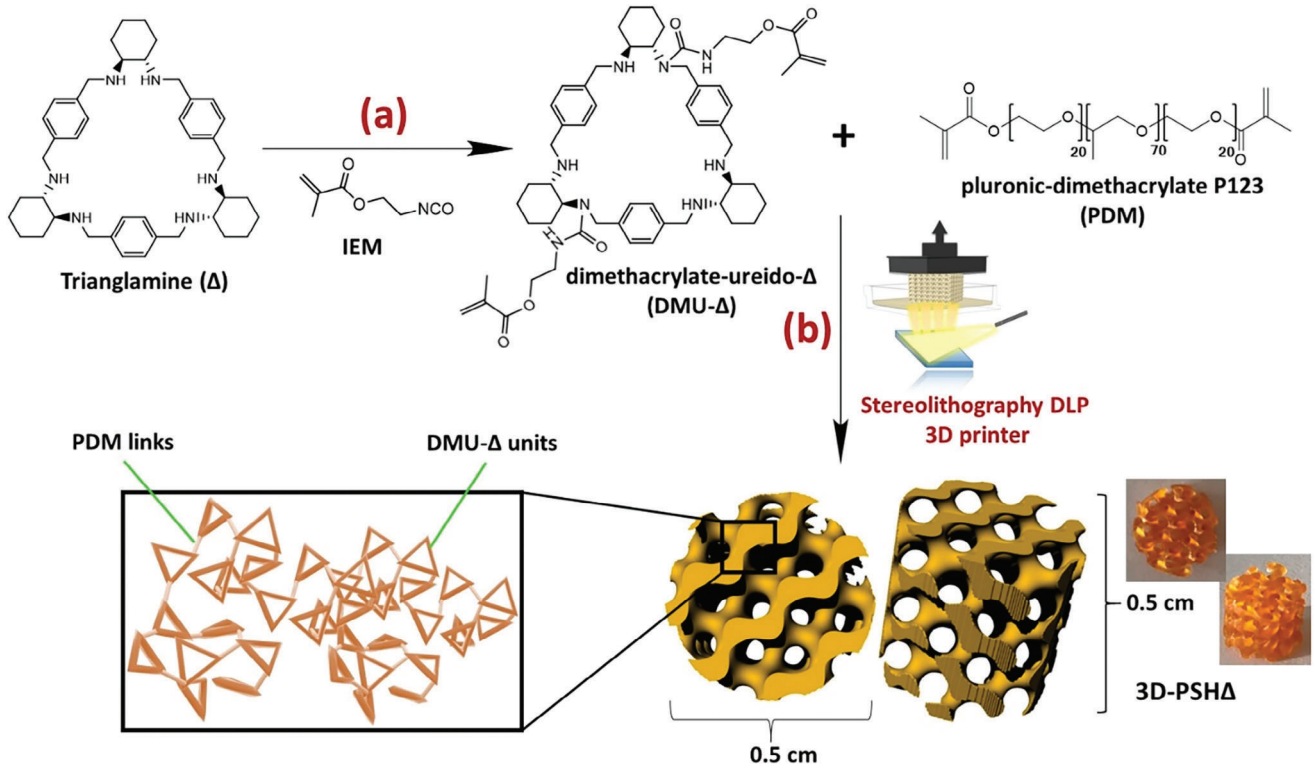

Scheme 1. a) Synthesis of the dimethacrylate-ureido-Δ (DMU-Δ), b) preparation of the 3D-PSHΔ hydrogels using SLA printing method.

the cross-linker (see Figure S9, Supporting Information for full molecular characterization).

The printable resin was prepared via mixing the DMU-Δ and the P123 dimethacrylate (PDM) (Scheme 1b). Samples containing varied ratios of DMU-Δ to PDM were prepared (**Figure 1**). Increasing the ratio of DMU-Δ to PDM increased the Young's modulus and the stress at break while the deformation at break was decreased. For example, increasing the DMU-Δ: PDM ratio from 10:90 to 50: 50, increased the Young's modulus from 0.36 to 1.12 MPa while the deformation at break decreased from 77 to 54%. Varying the amount of DMU-Δ in the resulting hydrogels has a very small effect on the water uptake. As observed, the swelling degree in water remained almost constant (≈ 3.1) regardless of the DMU-Δ content. In order to have a strong hydrogel with good water uptake as well as high amount of DMU-Δ the mass ratio of 1:1 DMU-Δ: PDM (representing 84:16 molar ratio) was chosen for the sorption tests.

As illustrated in Scheme 1, cylindrical hydrogels with gyroid pores were prepared using the stereolithography with DLP method. Gyroid architecture was chosen because of its high surface area (triply periodic minimal surface)[60] that could translate into a better surface contact and enhanced absorption capacity. Three hydrogels were prepared, a 3D porous hydrogel without Δ (3D-SH) as the control (100% of PDM), a 3D non-porous hydrogel trianglamine (3D-SHΔ), and a 3D porous hydrogel trianglamine (3D-PSHΔ). To maintain an equivalent amount of material in both designs, the external volume of the gyroid porous structure is fixed at 400 mm^3, whereas the non-porous hydrogels exhibit an external volume of 120 mm^3. The 3D-PSHΔ sample with high porosity ratio of 70% had a surface area of 540 mm^2 while this value for the non-porous sample was 140 mm^2. To test the performance of the prepared hydrogels, first, swelling kinetics in water

a/

Δ:P123	E at 3%(MPa)	σ (MPa)	ε (%)
0:100	0.23 ± 0.05	1.50 ±0.38	77 ± 2
10:90	0.36 ± 0.01	1.04 ± 0.15	70 ± 2
30:70	0.99 ± 0.11	2.04 ± 0.21	66 ± 1
50:50	1.12 ± 0.01	2.09 ± 0.25	54 ± 3

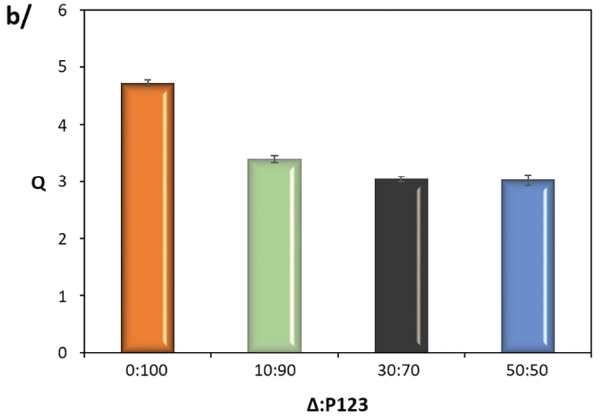

Figure 1. a) Evolution of mechanical performance and b) swelling ratio in water for hydrogel samples with varying Δ content.

and 1:1 water: ethanol solution was performed over 30 h (Figure S10, Supporting Information). In both cases, the porous hydrogel (3D-PSHΔ) reaches the equilibrium faster than the non-porous 3D-SHΔ (3 vs. 24 h). Additionally, as expected addition of ethanol resulted in more swelling as ethanol is a good solvent for DMU-Δ (unlike water).

To confirm the formation of the cross-linked hydrogel the FTIR spectra of 3D-PSHΔ was compared with the reactants PDM, IEM, DMU-Δ (Figure S11a, Supporting Information). In the spectra of the 2-isocyanoethyl methacrylate, the stretching vibration band at 2270 cm^{-1} corresponding to the isocyanate (N═C═O) disappears after the reaction with Δ, confirming the formation of DMU-Δ. Also, new signals emerge at ≈ 1710 and 1630 cm^{-1}, corresponding to the C═O stretch of carbonyl group, and to the N—H bending of secondary amine respectively, confirming the reaction between Δ and IEM. Additionally, in the 3D-PSHΔ spectrum, a stretching vibration band at 1100 cm^{-1}, corresponding to C—O—C, confirmed the presence of the PDM links within the 3D matrix (Figure S11b, Supporting Information). The thermogravimetric analysis (TGA) of DMU-Δ as well as the resulting hydrogels (3D-SH, and 3D-PSHΔ) are presented in Figure S12 (Supporting Information).

For the DMU-Δ, two weigh loss are observed; one between 230 and 310 °C (31.6%) corresponding to the IEM arms linked to the Δ and a second loss between 230 and 470 °C (54.24%), attributed to the degradation of the Δ. The 3D-SH start to decompose at 240 °C reaching complete degradation at 380 °C. In contrast, the temperature of the complete degradation of the 3D-PSHΔ is 100 °C higher (at 480 °C). This is not surprising as in our previous study, it was reported that increasing the molar ratio of the Δ as compared to the polymer linker results in enhanced thermal stability.[38] The small degradation step between 220 and 340 °C, corresponds to the degradation of the urea functionality in the DMU-Δ, as reported previously.[38] For a weight ratio of 50/50 between DMU-Δ and PDM, the calculated molar ratio indicates that 90% of the DMU-Δ is incorporated into the hydrogel structure. Nitrogen sorption experiments at 77 K on 3D-SHΔ, and 3D-PSHΔ showed no accessible micro- or meso-porosity in dry state with a negligible amount of adsorbed nitrogen (0.01 $m^2.g^{-1}$) (Figure S13, Supporting Information).

2.2. Biocompatibility Tests

In vitro biocompatibility of trianglimine, Δ, and DMU-Δ were tested on cells (Figure S14, Supporting Information). No toxicity was observed even at high concentration of 0.1 mM. In addition, in vivo biocompatibility of 3D-PSHΔ was evaluated in zebrafish embryos (Figure S15, Supporting Information). Gastrula stage embryos were maintained in water (4.5 mL $well^{-1}$) in presence of 3D-PSHΔ (27.75 mg) (Figure S15a,b, Supporting Information). Percentages of dead, chorionated and hatched embryos were analyzed at different hours post fertilization (hpf): 7, 24, 48, 72, and 120 hpf (Figure S15c, Supporting Information). Data demonstrated that 3D-PSHΔ did not induce any toxicity on embryos after 120 hpf of batching. No changes in mobility, morphology, and hatching rate were observed (Figure S15d, Supporting Information).

2.3. Sorption of PFOA from Deionized Water and River Water

To estimate the maximum uptake of PFOA by 3D-PSHΔ, isotherm studies were conducted with a concentration range of 5 to 200 ppm of PFOA at 25 °C. The results were fit using both Langmuir and Freundlich models using S2 (Figures S16 and S17, Supporting Information). Based on the correlated coefficient "R^2" obtained for each model in Tables S1 and S2 (Supporting Information), the sorption data could be fitted better using the Freundlich isotherm, implying a multi-layer sorption and sorption sites with different binding energies. Maximum sorption of 33.55 and 51.3 mg g^{-1} for 3D-SHΔ and 3D-PSHΔ were calculated using the Langmuir model (Tables S1 and S2, Supporting Information).

To gain a deeper insight into the sorption mechanism of PFOA in the prepared hydrogels (3D-SH, 3D-SHΔ, 3D-PSHΔ), kinetic experiments were conducted (**Figure 2a**). Comparing the sorption within the porous and non-porous 3D printed hydrogels with similar internal volumes (120 mm^3) provided valuable insight into the advantage of having a well-designed porous structure. Figure 2b illustrates the evolution of C_t/C_0 with various concentrations of PFOA over 24 h. The sorption efficiency of PFOA in deionized water was performed in triplicates using 3D-SH, 3D-SHΔ, and 3D-PSHΔ. The 3D-SH showed no PFOA uptake over 24 h, indicating that PDM does not interact with PFOA (Figure S18, Supporting Information). In contrast, the non-porous 3D-SHΔ adsorbed 88.0% and 83.3% of PFOA when initial concentrations of 5 and 0.5 ppm were used (Figure 2b). In the case of the porous 3D-PSHΔ (Figure 2b) almost all the PFOA was adsorbed (99.5% and 99.0% for both 5 and 0.5 ppm in 24 h).

To mimic real condition, the kinetic experiment was repeated in river water doped with PFOA (Figure 2c). The result suggests that PFOA sorption from river water was similar to the deionized water. The non-porous 3D-SHΔ, adsorbed 57.9% (5 ppm) and 83.0% (0.5ppm) of PFOA while the porous 3D-PSHΔ adsorbed 95.2% (5 ppm) and 98.7% (0.5 ppm) after 24 h. The slightly lower uptake in the case of river water is most probably due to the presence of diverse dissolved species (inorganic ions, pH level, organic matter, etc.). Studies have demonstrated that the presence of inorganic ions, pH level, and organic matter (OM) can disrupt PFAS adsorption by occupying active sites on the sorbent, leading to a reduction in adsorption capacity.[61–64]

To evaluate the transport process of the PFOA within the hydrogel, Fickian model was used. As shown in Scheme 1, n value of 0.45 suggests a diffusion based on concentration difference. And values of $0.5 < n < 1$ correspond to non-Fickian or anomalous transport where other driving forces would be involved. At $n = 1$, a Type II diffusion is considered where the solute migrates at a constant speed and is only controlled by the chain relaxation. The constant n and the diffusion coefficient D, were calculated according to Equation (2). **Table 1** summarizes the n values calculated for 3D-SHΔ and 3D-PSHΔ at 0.5 and 5ppm in deionized and river water. All the n values were between 0.67 and 0.89, suggesting a non-Fickian diffusion of PFOA within the hydrogel. This anomalous transport could be explained by the interactions between the DMU-Δ and the PFOA chains that would promote the migration of PFOA inside the hydrogel. In addition, the diffusion coefficients of 8.5×10^{-10} and 10^{-10} m^2 s^{-1} for 3D-PSHΔ and 3D-SHΔ indicates no influence of the medium concentration on

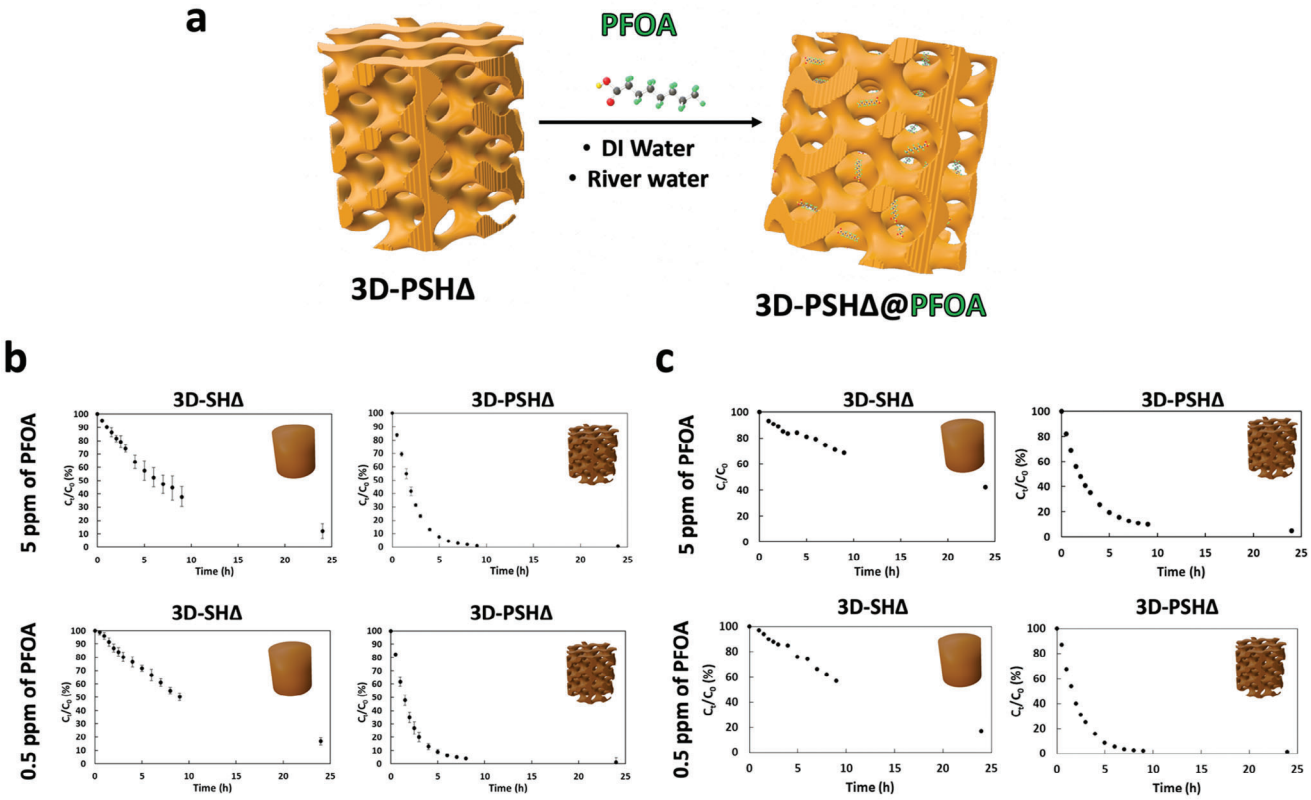

Figure 2. a) PFOA uptake from water and river water in 3D-PSHΔ b) Variation of C_t/C_0 as a function of time (h) for different concentrations of PFOA (5 and 0.5 ppm) in water with 3D-SHΔ and 3D-PSHΔ. c) Variation of C_t/C_0 as a function of time (h) for different concentrations of PFOA (5 and 0.5 ppm) in river water with 3D-SHΔ and 3D-PSHΔ.

the diffusion of PFOA. It is also important to evaluate the influence of the printing design on the swelling kinetics. In the case of the porous sample, the extraction of PFOA reached a plateau after 7–8 h while it took 24 h for the non-porous sample. This change can also be seen in the diffusion coefficient (20 times higher for the 3D-PSHΔ compared to the 3D-SHΔ). These results represent a notable enhancement of the kinetics in comparison to the performance of 3D-SHΔ. It is clear that the porous structure with higher surface area facilitates the diffusion of PFOA within the hydrogel as well as increasing the chance of contact between the functional cites and the PFOA chains leading to faster sorption kinetics.

Figure 3 depicts the PFOA uptake from both deionized water and river water at 5 and 0.5 ppm over 5 h. As it can be seen the porous structure (3D-PSHΔ) could adsorb a substantial amount of the PFOA from both deionized and river water, with respective percentages of 92.5%, 91%, 80.6%, and 91.5%. In contrast, 3D-SHΔ exhibited significantly lower uptake (42.4% to 24.2%) in both water sources. These results clearly show the benefit of using 3D printing of porous structures.

To determine the kinetic order and sorption parameters, experimental data were fitted into equations (S3) and (S4). The experimental results are presented in Supporting Information Figures S19–S26 (Supporting Information) and summarized in Tables S3–S10 (Supporting Information). Concerning the 3D-PSHΔ, pseudo-first and pseudo-second order models were found to be well-suited for describing the sorption kinetics, as evidenced by the high values of the correlation coefficient. Specifically, for

Table 1. Water diffusion parameters for 3D-PSHΔ and 3D-SHΔ in deionized and river water using the Fickian model.

		Deionized water		River water	
	PFOA ppm	*n*	D [m^2/s]	*n*	D [m^2/s]
3D-PSHΔ	0.5	0.89	5.9E-6	0.89	8.8E-6
	5	0.92	5.1E-6	0.93	8.6E-6
3D-SHΔ	0.5	0.76	3.3E-7	0.72	1.1E-6
	5	0.85	2.1E-7	0.65	0.9E-6

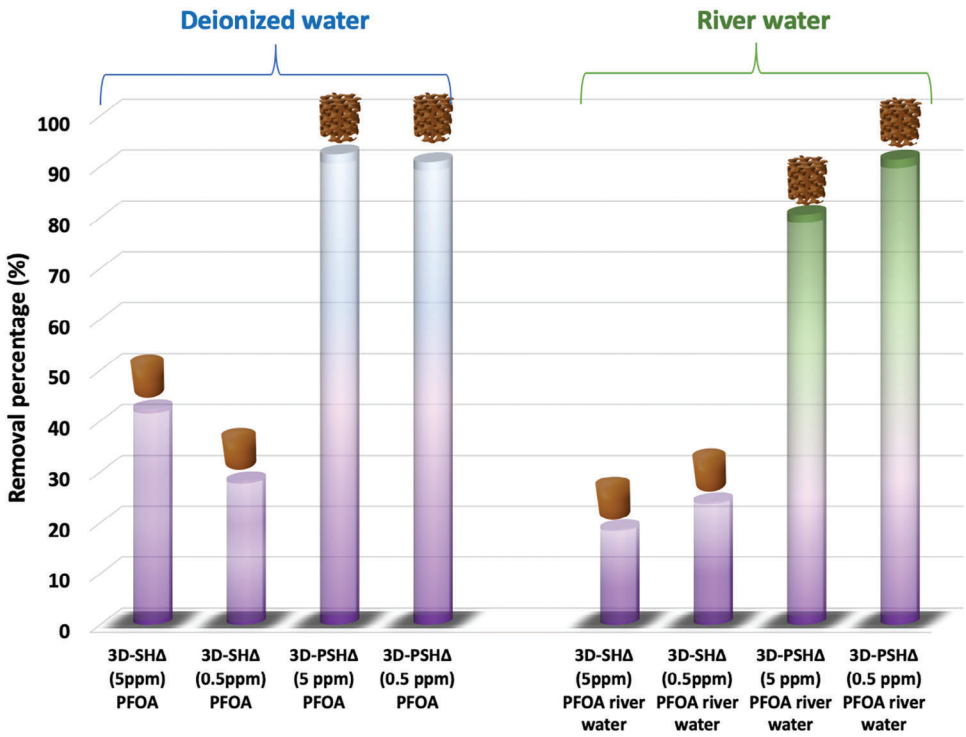

Figure 3. PFOA removal by 3D-SHΔ and 3D-PSHΔ with contact time of 5 h; [PFAS] = 5 and 0.5 ppm; [3D-SHΔ and 3D-PSHΔ] ≈ 40 mg.

the sorption of 5 ppm of PFOA, the correlation coefficients were $R^2 = 0.99$ and $R^2 = 0.99$ for the pseudo-first and pseudo-second order models, respectively (Figure S19, Supporting Information). Similarly, for the sorption of 0.5 ppm of PFOA, the correlation coefficients were $R^2 = 0.97$ and $R^2 = 0.99$ for the pseudo-first and pseudo-second order models, indicating a strong fit to the experimental data (Figure S20, Supporting Information). However, upon comparing the equilibrium sorption capacity (q_e) with the experimentally ($q_{e\,exp}$), it becomes clear that the pseudo second order model is a closer fit than the pseudo-first order model for both concentrations of 5 and 0.5 ppm (Tables S3 and S4, Supporting Information). These results suggest that the diffusion of PFOA to the sorption sites of Δ is not the main rate-limiting step. However, the kinetic sorption data for the non-porous hydrogel (3D-SHΔ) were better fitted with the pseudo-first-order model than with the pseudo-second order model. This choice is supported by higher correlation coefficients ($R^2 = 0.97$ for 0.5 ppm and $R^2 = 0.99$ for 5 ppm) compared to the values obtained from the pseudo-second order model (Figures S21 and S22, Supporting Information). Furthermore, upon comparing q_e with $q_{e\,exp}$ the data consistently aligns in the same direction, thereby affirming the validity of the pseudo-first order model for both concentration (Tables S5 and S6, Supporting Information). As a matter of fact, these results revealed that the diffusion of PFOA to the active sites of the Δ is the rate controlling step. This phenomenon is likely attributed to the non-porous structure of the hydrogel. The 3D-PSHΔ tested in river water also follow both the pseudo-first and pseudo-second order models. The sorption of 5 ppm of PFOA, showed the correlation coefficients were $R^2 = 0.99$ for both models (Figure S23, Supporting Information). On the other hand, the sorption of 0.5 ppm of PFOA, the correlation coefficients were $R^2 = 0.99$ and $R^2 = 0.98$ for the pseudo-first and pseudo-second order models (Figure S24, Supporting Information). Once again, the q_e confirmed the pseudo-second order kinetics. This is supported by a consistent close value observed for both concentrations (Tables S7 and S8, Supporting Information). The non-porous hydrogel, 3D-SHΔ, fitted with pseudo-first order model. This choice is supported by higher correlation coefficients ($R^2 = 0.97$ for 5 ppm and $R^2 = 0.97$ for 0.5 ppm) compared to the values obtained from the pseudo-second-order model and supported by the q_e compared to the $q_{e\,exp}$ (Figures S25 and S26; Tables S9 and S10, Supporting Information). These results indicated identical outcomes for both materials (3D-PSHΔ and 3D-SHΔ) when subjected to either deionized or river water for PFOA removal. We confirmed that the hydrogel with porous structure exhibited distinct behavior and modeling compared to its non-porous structure.

FTIR and TGA were performed to detect the adsorbed PFOA. 3D-PSHΔ was first immersed in an aqueous solution of PFOA (200 ppm) for 24h and dried at 60 °C to form 3D-PSHΔ@PFOA. Figure S27 (Supporting Information) presents the ATR-FTIR spectra of the material before and after adsorption. Strong bands at 1200 and 1237 cm^{-1} corresponding to the ν (C—F) stretching vibration of PFOA are visible in both PFOA and 3D-PSHΔ@PFOA, confirming the presence of PFOA.[65] A shift of the ν(C═O) stretch from 1754 cm^{-1} in PFOA to 1684 cm^{-1} in 3D-PSHΔ@PFOA is also observed and is likely due to the loss of the proton from the carboxylic acid function to form a carboxylate group.[66] TGA analysis of 3D-PSHΔ@PFOA revealed a noticeable weight loss between 100 and 170 °C. This few percentages of weight reduction corresponds to the sorption of PFOA by the 3D-PSHΔ material (Figure S28, Supporting Information).

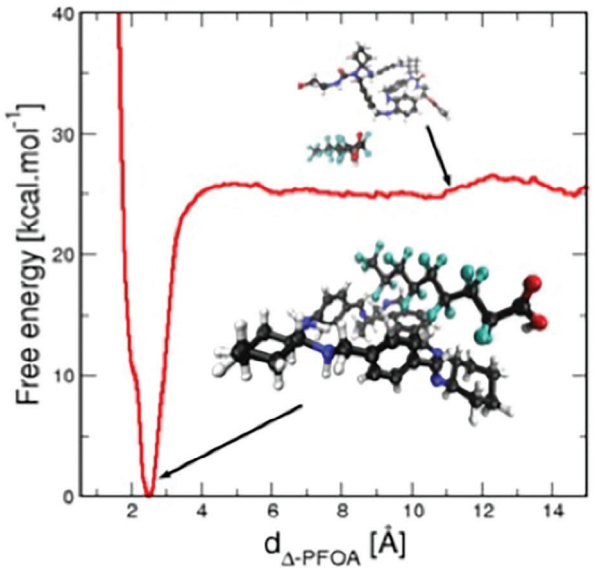

Figure 4. Free energy curve as a function of the intermolecular distance between PFOA and Δ. Two snapshots are represented to visualize how molecules are organized on the sorption site and at a mid-range distance.

2.4. Metadynamic Simulations between Δ and PFOA

To gain further understanding of the sorption of PFOA within the 3D-PSHΔ and more precisely with the Δ, dynamic molecular simulation was performed to elucidate the interaction between the two entities. The sorption pathway's energy landscape was investigated through molecular metadynamics, an enhanced sampling approach,[67,68] as detailed in the Supplementary Information. The study focused on observing the repeated sorption and desorption of PFOA on the Δ. The model comprised one PFOA molecule and one Δ immersed in 2000 water molecules and the system size was $2 \times 2 \times 2$ nm^3. A force field with adaptable charges, ReaxFF,[69–71] has been used in order to take into account local charge transfers in the vicinity of water molecules and when PFOA is adsorbed on the Δ. The intermolecular distance between PFOA and Δ has been used to bias and enhance the dynamics so that multiple sorption and desorption are observed within 1 ns of simulation (Figure S29, Supporting Information).

Our simulations revealed that PFOA physically adsorbs onto the Δ through F…H electrostatics and van der Waals interactions, with the interaction at the PFOA head not being particularly favored. This suggests that the fluorocarbon chain length may influence the sorption energy. Following 5 ns of metadynamic simulation, the energy barrier converged to 3 kcal mol^{-1} for sorption and 25 kcal mol^{-1} for desorption, indicating good capture ability and a possible reversible process (**Figure 4**). This finding aligns with experimental results demonstrating good reversibility. The sorption site was identified at 2.5 Å from the Δ. In the most stable configuration, the PFOA is aligned in parallel with one of the branches of the Δ maximizing the number of H…F interactions. This is confirmed through a comparison of the sorption energy for PFOA and PFPrA: PFPrA does not form as many H…F bonds with the Δ structure. As a result, as depicted in Figure S30 (Supporting Information), PFPrA exhibits a sorption energy of ≈3 kcal mol^{-1}, which is lower than that of PFOA, which is 25 kcal mol^{-1}. After analyzing the results of the metadynamic simulation, we can assert that the Δ significantly contributes to the capture of PFOA. Considering the Δ molecular weight, which is ≈86% into the hydrogel compared to PDM, it is reasonable to estimate an uptake of ≈ 60 and ≈ 40 mg g_{Δ}^{-1} for 3D-PSHΔ and 3D-SHΔ, respectively.

2.5. Material Stability and Regeneration/Reuse

The stability, and recyclability of the prepared sorbents were tested in different pH conditions 1M HCl and 1M NaOH (Figure S31, Supporting Information). It was observed that the 3D-PSHΔ didn't swell much in basic solution while it swelled significantly in acidic environment (suggesting a heightened affinity for chloride ions). Furthermore, 3D-PSHΔ exhibited no signs of degradation even after three-months in such environments. A significant benefit of using hydrogels would be the possibility of regenerating and re-using the sorbents. Here, a simple and efficient regeneration process is employed; stirring the 3D-PSHΔ in a mixture of ethanol and deionized water (50 v/v%) at room temperature for 24.

As previously discussed (Figure S11, Supporting Information), immersion in a 50% ethanol aqueous solution leads to substantial swelling of the hydrogel, affirming its affinity for the solvent. This hydrogel expansion contributes significantly in accelerating the desorption of the adsorbed PFAS. Consequently, this solvent was used for removing the adsorbed PFAS overnight. The sorption/ desorption cycles were repeated 5 times, without any loss of sorption capacity or structure (**Figure 5**). These results prove the potential of the 3D-PSHΔ for long-term use of the porous shaped hydrogel-based trianglamine for PFOA removal. Additionally, we reported the sorption and desorption of PFOA in mg (Figure S32, Supporting Information). At an initial concentration of 5 ppm, 0.25 mg of PFOA was adsorbed, with ≈60% of the adsorbed PFOA being desorbed during each regeneration cycle, leaving 40% of PFOA still attached to the material, indicating a strong interaction between the two. In contrast, when using 0.5 ppm as the initial concentration, over 85% of the captured PFOA was desorbed.

2.6. Kinetic Sorption of Several PFAS with 3D-PSHΔ and 3D-PSHΔQ$^+$

The metadynamic simulations demonstrated that the interaction between and PFOA, stems from hydrogen bonds between the protons of the aromatic groups of the Δ and the fluoride groups of PFOA. However, another notable interaction for adsorbing PFAS appears to be the electrostatic forces.

Research indicates that the positive charge from the amino groups in sorbents plays a crucial role, facilitating the sorption of PFAS through electrostatic attraction within a timeframe ranging from 4 to 48 h.[72] Recently, adsorbents such as polyaniline nanotubes[73] and quaternized cotton[74] have demonstrated remarkable sorption capacity for PFOA and PFOS. Following the same logic, to enhance the PFAS sorption, permanent positive charges were introduced in the 3D-PSHΔ using iodomethane

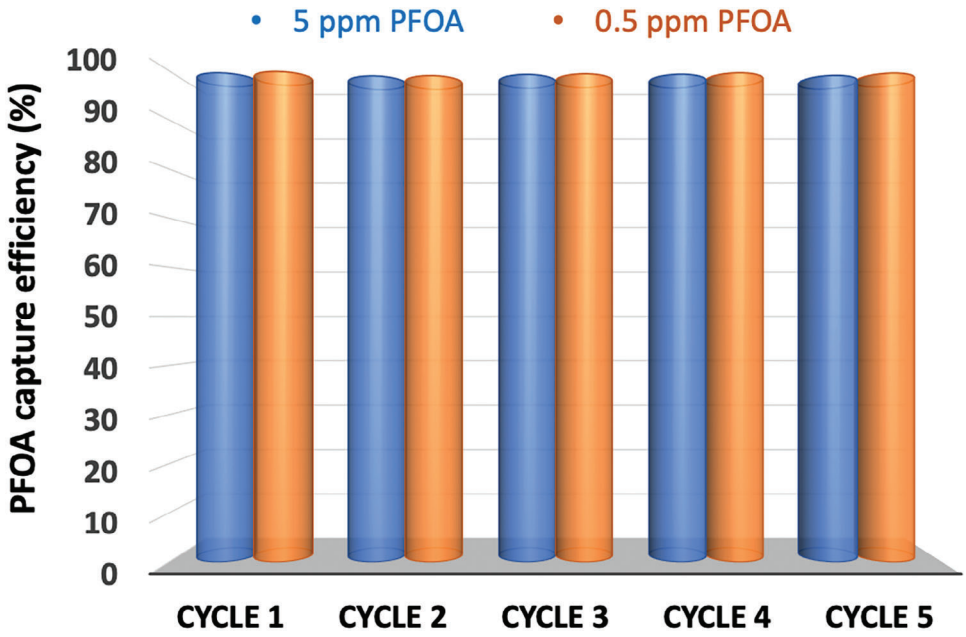

Figure 5. 3D-PSHΔ efficiency in removing PFOA through sorption/desorption recycles.

(quaternization of the free secondary amine of the Δ to generate 3D-PSHΔQ$^+$) (**Figure 6**). The positively charged 3D-PSHΔ (3D-PSHΔQ$^+$) was analyzed by Raman spectroscopy (Figure S33a,b, Supporting Information). The Raman spectrum revealed multiple peaks corresponding to iodide ions originating from the iodomethane reagent, thereby confirming the dissociation of iodine and methane. Specifically, peaks at 111 and 130 cm^{-1} were identified and attributed to the symmetric (ν1) and asymmetric (ν2) stretching frequencies of I_3^- anions into the 3D-PSHΔQ$^+$. To go further, the synthesized sorbents (3D-PSHΔ and 3D-PSHΔQ$^+$) were tested with a series of PFAS: PFOA, PFHpA, PFHxA, PFPeA, PFOS, and PFBS. The short-chain PFAS exhibit greater ubiquity, enhanced mobility within the environment, increased resistance to degradation and removal compared to the long-chain PFAS. Here, PFOA and PFOS were chosen to represent long chain PFAS, whereas PFHpA, PFHxA, PFPeA, and PFBS were chosen to represent short-chain PFAS. An initial concentration of 0.0012 mmol L^{-1} in deionized water was prepared for each PFAS: 0.5 ppm for PFOA, 0.44 ppm (0.0012 mmol L^{-1}) for PFHpA, 0.38 ppm (0.0012 mmol L^{-1}) for PFHxA, 0.32 ppm (0.0012 mmol L^{-1}) for PFPeA, 0.6 ppm (0.0012 mmol L^{-1}) for PFOS, and 0.36 ppm (0.0012 mmol L^{-1}) for PFBS. The contact time was for this series of kinetics was fixed at 24 h. Results indicated significant uptake (92%, 95%, 88%, 83%, 96%, and 95% for PFOA, PFHpA, PFHxA, PFPeA, PFBS, and PFOS, respectively) (Figure S34 (Supporting Information). In the next series of tests, the contact time was reduced to 300 min. After this contact time, 3D-PSHΔ took up 91, 76, 69, and 65% for PFOA, PFHpA, PFHxA, and PFPeA, respectively (Figure 6a). It can be seen that the shorter PFAS chains were adsorbed less. This observation is in agreement with the metadynamic simulation results indicating that the driving force in the process of sorption is the hydrophobic interactions. Regarding the different charged head groups, the sulfonated PFAS, both PFOS and PFBS were adsorbed the same (76%) regardless of their chain length. The tests with the quaternized sorbents (3D-PSHΔQ$^+$), under the same conditions (concentration, deionized water, and 24 h contact time) resulted in almost 100% removal of all the six tested PFAS (99, 99, 98, 93, 99, and 99% for PFOA, PFHpA, PFHxA, PFPeA, PFOS, and PFBS) (Figure S35, Supporting Information). The remarkable enhancement in both kinetic and removal capacity could be attributed to of the permanent positive charges within the hydrogel, leading to heightened electrostatic interactions. Figure 6b, shows the capacity of 3D-PSHΔQ$^+$ after 300 min of contact time. Impressive capture rates (90%, 91%, 88%, and 89% for PFOA, PFHpA, PFHxA, and PFPeA) were reached. Unlike the 3D-PSHΔ, the 3D-PSHΔQ$^+$ has the same removal capacity for all the tested with various chain lengths. This underscores the advantageous impact of quaternization for PFAS removal. However, when examining sulfonic PFAS, 3D-PSHΔQ$^+$ showed 95% removal efficiency for PFOS and 74% for PFBS. The observed differences in removal efficiency can be attributed to the varying chain lengths of PFAS, highlighting the nuanced effects of quaternization on different compounds. In addition, 3D-PSHΔQ$^+$ exhibited a more efficient uptake of PFOS compared to PFOA after 5 h contact time. This result can be attributed to the higher acidity of the sulfonic group compared to the carboxylic group. Consequently, it suggests that the PFOS has a higher affinity for the surface of the quaternized hydrogel. Moreover, kinetic order model of the PFAS sorption with the 3D-PSHΔ, 3D-PSHΔQ$^+$ are presented in the supporting information (Figures S36–S41, Supporting Information).

Applying Fickian model on 3D-PSHΔ and 3D-PSHΔQ$^+$ in the presence of the various PFAS, the constant n value and the different diffusion coefficient were calculated as summarized in Table S11 (Supporting Information). Across all tests, n value lies in the range between 0.5 and 1 which de-scribes a non-Fickian diffusion mechanism validating the presence of an interaction between all

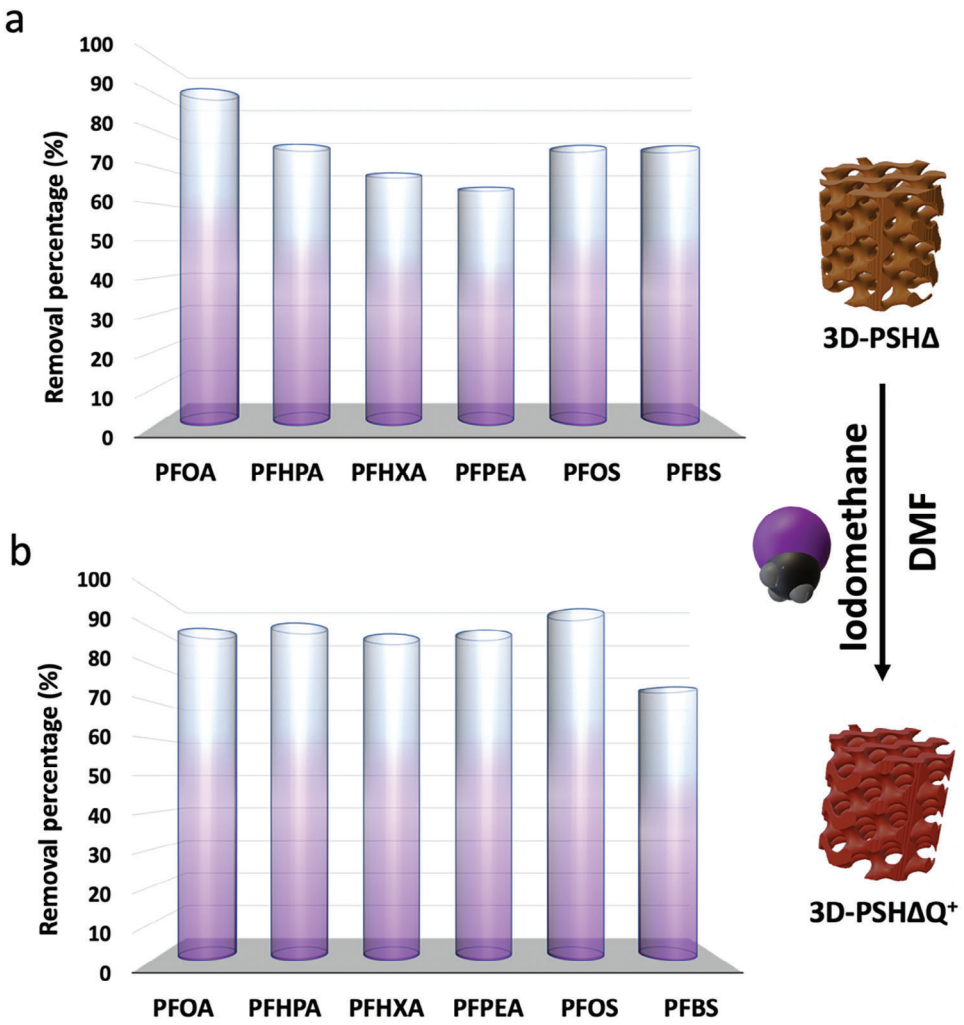

Figure 6. a) PFAS removal by 3D-PSHΔ with 5 h of contact time; [PFOA] = 0.5 ppm, [PFHpA] = 0.44 ppm, [PFHxA] = 0.38 ppm, [PFPeA] = 0.32 ppm, [PFOS] = 0.6 ppm, [PFBS] = 0.36 ppm; [3D-PSHΔ] = 40 mg, b) PFAS removal by 3D-PSHΔQ+ with 5 h of contact time; [PFOA] = 0.5 ppm, [PFHpA] = 0.44 ppm, [PFHxA] = 0.38 ppm, [PFPeA] = 0.32 ppm, [PFOS] = 0.6 ppm, [PFBS] = 0.36 ppm; [3D-PSHΔQ$^+$] ≈ 60 mg.

the different PFAS and the Δ in the hydrogel as much as in deionized water than river water (Table S11, Supporting Information).

3. Conclusion

In summary, an efficient, reusable, and non-toxic porous adsorbent is prepared for the removal of PFAS from water. This work demonstrates the promise of using SLA 3D printer to prepare porous-shaped hydrogels to improve the kinetics and the uptake capacity of a range of PFAS. The study revealed that 3D-SH without any Δ has no affinity toward PFOA. While the 3D-PSHΔ showed a remarkable uptake capacity through fast kinetics. This indicates the key role of Δ in capturing PFAS. In addition, the designed porous structure allowed higher contact surface generated by the SLA enhancing the sorption. During 5 h contact, 3D-PSHΔ was able to remove 92.5 and 91% of PFOA instead of 42.4 and 28.3% for 3D-SHΔ for 5 ppm and 0.5 ppm, respectively. The 3D-PSHΔ demonstrated thermal and chemical stability. Furthermore, the 3D-PSHΔ could be regenerated and reused over several cycles without any loss of performance. The maximum uptake for 3D-PSHΔ was estimated at 60 mg of PFOA per g of Δ (considering the amount of Δ within the hydrogel). In addition, metadynamic simulations elucidated the mechanism of PFOA sorption and the importance of the hydrophobic interactions between the fluorinated chain of PFOA and the Δ. 3D-PSHΔ was tested with a range of various PFAS. The results showed that when the PFAS chain length decreases the kinetic and the removal percentage decreases. In order to improve the PFAS uptake, the hydrogel was chemically modified to generate have permanent positive charge. The results showed much faster kinetics and higher capacity of sorption as compared to the 3D-PSHΔ for all the six tested PFAS. In order to benchmark the performance of this new functional material, the percentage removal of PFOA and PFOS was compared with various materials reported in the literature **Figure 7** (Table S12, Supporting Information). When compared to a range of diverse material such as granular activated carbon (GAC), resins, multi-walled carbon nanotubes, polymers based-cyclodextrin, quaternized cotton, covalent organic

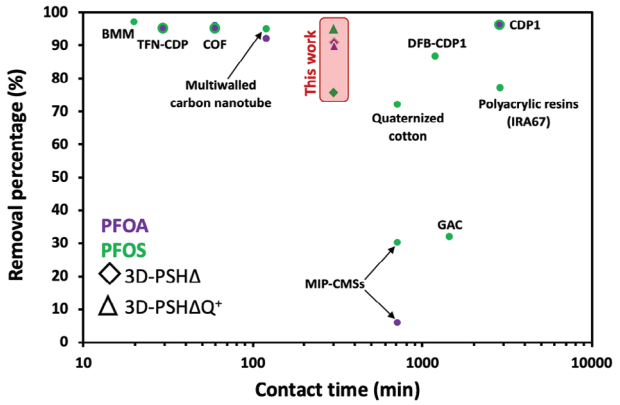

Figure 7. The comparison of performance of different material in adsorbing PFOA and PFOS.

frameworks (COFs) among others, it is evident that both 3D-PSHΔ and 3D-PSHΔQ$^+$ are very efficient in removing PFAS. In addition to its remarkable performance, this new material is easy to produce, and its non-powder form allows for straightforward regeneration and operation under low-energy conditions. Notably, the synthesis of the Δ is comparatively simple, enabling kilogram-scale production. To achieve a broader environmental impact, further optimization of the 3D printing technique is essential. While initial applications may target industrial wastewater treatment, future developments could expand to groundwater remediation. Despite these challenges, the scalability and efficiency of this material position it as one of the most efficient options for adsorbing various types of PFAS.

4. Experimental Section

Materials and Methods: All reagents were purchased from commercial suppliers and used without further purification. (±)-trans-1,2-diaminocyclohexane, terephthalaldehyde, triethylamine, sodium borohydride, Pluronic P123, perfluorooctanoic acid (PFOA), perfluoroheptanoic acid (PFHpA), perfluorohexanoic acid (PFHxA), perfluoropentanoic acid (PFPeA), perfluorooctanesulfonic acid (PFOS), perfluorobutanesulfonic acid (PFBS), were purchased from Sigma Aldrich. 2-isocyanatoethyl methacrylate was purchased from TCI.

^{1}H NMR and ^{13}C NMR spectrum were recorded on Bruker Avance III 400 MHz NMR spectrometers in $CDCl_3$.

Mass spectrometric (MS) analyses were performed with SYNAPT G2-S (Waters Corporation, Manchester, UK) equipped with an ESI source. High-resolution electrospray ionization mass spectrometry (ESI-HRMS) was acquired in positive or negative ion mode. Conditions: capillary voltage 3000 V; cone voltage 20V, dry gas temperature 140 °C, de-solvation temperature = 450 °C, dry gas flow, 1000 L.h^{-1} and nitrogen as nebulizer gas, Pressure = 6.5 bars. 1ng µL^{-1} Leucine Enkephalin was used as standard for internal calibration.

Thermogravimetric analysis (TGA) was measured using TA Instruments SDT Q600 by heating the sample to 700 °C under nitrogen (60 mL min^{-1}) at a heating rate of 20 °C min^{-1}.

FT-IR analysis was made on a Thermo Nicolet Nexus FTIR spectrometer with diamond ATR attachment. Samples were subjected to 32 scans in the range of 4000 cm^{-1} and 650 cm^{-1}.

3D Printed structures were constructed by stereolithography printer with a digital light processing (DLP) (Asiga Max X27, Asiga Australia). The resin was prepared by dissolving the appropriate amounts of DMU-Δ and pluronic dimethacrylate P123 at a mass ration 1:1 in benzyl alcohol (50 w/w%). Lithium phenyl-2,4,6-trimethylbenzoylphosphinate (LAP) was added at 2.5 w/w% with respect to the monomers as photoinitiator. To ensure a high-resolution printing, Orange G was added at 0.1 w/v% as photo-absorber. UB intensity was fixed at 20 mw cm^{-2} and the irradiation time was set at 40s in order to obtain a 100µm layer thickness. Porous and non-porous cylinders were printed having the same solid volume of 100µL. The samples were washed gradually with water in 48h to remove any unreacted species and then dried under vacuum at room temperature for 24h (until constant weight).

Swelling Capacity of the hydrogels was measured by submerging the dry samples in 30 mL Milli-Q water and measuring the mass at different time intervals until constant mass at room temperature (20 °C). The swelling degree (Q) is calculated using the following equation:

$$Q = \frac{m_{swollen\ at\ time\ t}}{m_{dry}} \quad (1)$$

Compressing tests were performed on an Instron 3366L5885 mechanical tester equipped with a 100N load cell. The samples were the 3D printed cylinder at their equilibrium swelling degree in water. The compression speed was set at 1 mm.s^{-1} with a 200 ms sampling time. Each value is presented by the mean ± standard deviation (n = 3). The Young's modulus is calculated is the slope of the stress-strain curve at 3% deformation.

Fickian model was used to study the diffusion mechanism of PFAS into the hydrogel. From the sorption kinetics, the data is fitted using Equation (1) where t is the time, C_t is the concentration at time t, C_0 is the initial concentration of PFAS, k is the characteristic constant of the hydrogel and the n the constant describing the PFAS diffusion mechanism.

$$\frac{C_t}{C_0} = k \,.\, t^n + 100 \quad (2)$$

Diffusion coefficient was determined using equation X where D is the diffusion coefficient in m^2/s, S is the specific area of the hydrogel in contact with water (equal to 0.00054 and 0.00014 m^2 for the porous and non-porous structure respectively) and *k'* the characteristic constant obtained when fitting the sorption data with $n = 0.5$ for the first 20% only.

$$k' = 4 \,.\, \left(\frac{D}{S}\right)^{0.5} \quad (3)$$

LC-MS/MS analysis was made on a Shimadzu – LCMS-8050 triple quadrupole

Synthetic procedures and characterizations of Δ, PDM and DMU-Δ: The compounds trianglamine (Δ), P123 dimethacrylate (PDM) and dimethacrylate-ureido-trianglamine (DMU-Δ), have been synthesized following the general procedure below:

Synthesis of trianglamine (Δ): A mixture of (±)-trans-1,2-diaminocyclohexane (2.28 g, 20 mmol), terephthalaldehyde (2.68g, 20 mmol) was added with triethylamine (7.0 mL, 50 mmol) and stirred overnight in 200 mL methanol. The mixture was cooled in an ice bath and sodium borohydride (2.28 g, 60 mmol) was added over 1 h to reduce the trianglimine to trianglamine. After 3 h stirring at room temperature, the solvents were removed under vacuum and the residue was dissolved in dichloromethane (100 mL) and washed with aqueous sodium carbonate (5%) and water. The organic extract was dried over magnesium sulfate then the solvent was evaporated and the product was dried under vacuum at 50 °C for 5 h. The obtained yield was 90% (4 g). In order to obtain pure trianglamine, the macrocycle was solubilized in 4 mL of absolute ethanol (EtOH). A solution of 10 mL of absolute EtOH with 2 mL of concentrated HCl (37%) was added dropwise to the mixture. The formation of Δ.HCl as a white precipitate was observed during the addition. The solid Δ.HCl was filtered and dried under vacuum. The white solid was dissolved in water and the pH was increased using 20 mL of 2 M NaOH solution. This treatment resulted in formation of a white precipitate. The pure precipitated trianglamine (Δ) was filtered and dried under vacuum for 24 h at 50 °C.[34]

Trianglamine (Δ): ^{1}H NMR ($CDCl_3$, 400 MHz) δ (ppm) = 7.3 (d, 12H), 3.9 (d, 6H), 3.6 (d, 6H), 2.30 (m, 6H), 2.25 (m, 6H), 1.75 (m, 6H), 1.1-1.3 (m, 12H); 13C NMR ($CDCl_3$, 400 MHz) δ (ppm) = 25, 32, 51, 61, 128, 139; FTIR (cm^{-1}) = 3290 (NH, stretch), 2922 (Caromatic-H, stretch), 2850 (Calkane-H, stretch), 1201 (C-N); MS Cal. = 648.5, ESI-MS found for Δ [M+H+]+ = 649.5. Elem. Anal. Cal. 77.73% C, 9.32% H, 12.95% N.

Synthesis of P123 dimethacrylate (PDM): P123 dimethacrylate was obtained by grafting methacrylate moieties on the hydroxyl chain ends in the presence methacrylic anhydride (MA) and triethylamine (TEA). Pluronic P123 was dissolved in DCM at 70 w/w%. under magnetic stirring. Upon complete dissolution, 3 equivalents of TEA were added with respect the hydroxyl group then the solution was left to stir for 2 h. Finally, 3 eq of MA were added with respect to the hydroxyl groups. The reaction was done in an ice bath for 24h. The methacrylated pluronic was then purified after 3 days dialysis in 500 DA membrane against distilled water while changing the water twice a day. Purified Pluronic P123 was recovered by freeze drying.

Synthesis of dimethacrylate-ureido-Δ (DMU-Δ): The trianglamine 3.72 g (0.0058 mol) was dissolved in 60 mL of dichloromethane and added to a round bottom flask. Then, a solution of 2 eq of the 2-isocyanatoethyl methacrylate (1.81 g, 0.0116 mol) in 10 mL of dichloromethane was added drop-wise to the round bottom flask. The reaction mixture was stirred overnight at room temperature. Then, the solvent (dichloromethane) was removed under vacuum and dried under reduced pressure to lead to the desired product with a yield of 98%.

Dimethacrylate-ureido-trianglamine (DMU- Δ): 1H NMR ($CDCl_3$, 400 MHz) δ (ppm) = 7.3 (d, 12H), 6.01 (d, 1H), 5.51 (d, 1H), 4.16 (t, 2H) (3.9 (d, 6H), 3.6 (d, 6H), 3.4 (t, 2H), 2.30 (m, 6H), 2.25 (m, 6H), 1.87 (t, 3H), 1.75 (m, 6H), 1.1-1.3 (m, 12H); 13C NMR ($CDCl_3$, 400 MHz) δ (ppm) = 18.4, 24.64, 25.09, 25.77, 32, 40, 51, 61, 125, 127, 128, 136, 139, 167; MS Cal. = 957.6, ESI-MS found [M+H+]+ = 959.6.

Quaternization of the 3D-PSHΔ (3D-PSHΔQ^+): The quaternization of the 3D-PSHΔ was performed by immersing/swelling the dry 3D-PSHΔ in a solution of 10 mL of dimethylformamide containing 20 eq (0.262 mL) of iodomethane compared with the amine groups of the DMU- Δ. After 24 h, the hydrogels were picked up and immersed in water for 3 days and the water was changed after each 12 h in order to exchange DMF with water for easier drying. Then, the hydrogels were dried in oven at 35 °C under vacuum.

Isotherm Sorption of PFOA with 3D-SHΔ, and 3D-PSHΔ: 10 solutions of varying PFOA concentrations were prepared: S1 (200ppm), S2 (180ppm), S3 (160 ppm), S4 (120ppm), S5 (100ppm), S6 (80ppm), S7 (50ppm), S8 (20ppm), S9 (10ppm) and S10 (5ppm). Each solution was diluted to a final concentration of 5ppm, with dilution factors as follows: S1 (40), S2 (36), S3 (30), S4 (24), S5 (20), S6 (16), S7 (10), S8 (4), S9 (2), and S10 (1). The experiments were conducted on 20 mL solutions over a 24-h period.

For the 3D-SHΔ samples, ≈30 mg of material was used, and for the 3D-PSHΔ samples, ≈50 mg was used.

Sorption Kinetic of PFOA with 3D-SH, 3D-SHΔ, and 3D-PSHΔ: *Experiments in DI water*: Solutions containing 5 and 0.5 ppm of perfluorooctanoic acid (PFOA) were meticulously prepared. In a 1L volumetric flask, 200 mg of PFOA was added and thoroughly mixed overnight to ensure its complete dissolution, resulting in a 200 ppm PFOA solution in deionized (DI) water. Subsequently, we performed dilutions of the original solution (200 ppm) to achieve concentrations of 5 ppm (6.25 mL of the 200 ppm solution into 250 mL volumetric flask) and 0.5 ppm (0.625 mL of the 200 ppm solution into 250 mL volumetric flask), allowing for precise control and calibration in our experimental setup.

The experiments were conducted in 75 mL beakers containing 50 mL of 5 or 0.5 ppm of perfluorooctanoic acid (PFOA) in deionized (DI) water. Kinetic sorption studies were carried out using three different materials: 3D-SH (≈10mg), 3D-SHΔ (≈38mg), and 3D-PSHΔ (≈48mg). Each experiment spanned a 24-h duration, with sampling intervals of 30 min for the initial 3 h, followed by hourly sampling until the completion of the 24-h period. To ensure robustness and accuracy, triplicate experiments were performed for each material and concentration (5 and 0.5 ppm).

Experiments from the river water: (river water collected form Le Lez, Saint-Clément-de-Rivière, France). The collected river water was filtered with 0.22 µm Teflon membrane in order to remove the large species such as microorganism. Then, the water was doped with a precise amount of PFOA in order to obtain 5 and 0.5 ppm PFOA. In a 1L volumetric flask, 200 mg of PFOA was added and thoroughly mixed overnight to ensure its complete dissolution, resulting in a 200-ppm PFOA solution in deionized (DI) water. Subsequently, dilutions were performed to prepare 5 ppm (6.25 mL of the 200 ppm solution into 250 mL volumetric flask of river water) and 0.5 ppm (0.625 mL of the 200 ppm solution into 250 mL volumetric flask of river water.

The experiments were conducted following the above described method for the DI water.

A concentration ranging from 5 to 200 ppm of PFOA was used to investigate sorption isotherms based on Langmuir and Freundlich model. Langmuir model considers monolayer sorption of the adsorbate and homogeneous distribution of the sorption site. The following equation presents the linear form:

$$C_e/q_e = C_e/q_m + 1/(q_m K_L) \quad (4)$$

where C_e is the concentration at the equilibrium, q_e is the quantity sorbed at the equilibrium; q_m is the maximum quantity adsorbed, and K_L is the Langmuir constant.

Freundlich model considers the binding sites of the adsorbent heterogeneous, and the sorption is multilayer. The following equation presents the linear form:

$$ln(q_e) = lnK_f + (1/n)\, lnC_e \quad (5)$$

where K_f is a Freundlich constant, and 1/n is the heterogeneity factor.

The sorption kinetic were analyzed by pseudo-first order model and pseudo-second order model by fitting the experimental data into their linear from consecutively (Equations (6) and (7)):

$$ln(q_e - q_t) = ln(q_e) - k_1 t \quad (6)$$

$$t/qt = 1/(K_2 q^2{}_{e)} + 1/q_e \quad (7)$$

where q_e is defined as the equilibrium sorption capacity, K_1 (min^{-1}) is the constant of the pseudo-fisrt order model, and k_2 (g mg^{-1} min^{-1}) is the constant of the pseudo-second order model.

Metadynamics Simulation Details: Metadynamics is an enhanced sampling approach based on molecular dynamics. Enhanced sampling was done by the means of so-called collective variables that guides the system along the reaction path and describes it. In this work, we have performed metadynamics in the NPT ensemble using LAMMPS package with an integration time step of 0.1 fs in order to ensure a good water dynamic. The thermostat damp factor is 100 fs and the barostat damp factor is 1 ps. The forces have been evaluated using ReaxFF, which enables charge evolution during the dynamics and chemical reactions. We have used a set of parameters for ReaxFF that has been optimized for CHONF elements on various organic molecules [https://journals.aps.org/prb/abstract/10.1103/PhysRevB.87.104114 and https://www.sciencedirect.com/science/article/pii/S0301010420302469?via%3Dihub#b0210]. Note that in our work, we are not simulating chemical reactions. We have used a single collective variable in order to optimize the sampling of the sorption pathway which is the closest distance between any atom of the trianglamine macrocycle and any atom of the PFOA molecule. Therefore, the molecules are free to orientate and adapt to find the most efficient sorption site without favoring any sorption site. The well-tempered metadynamics approach has been used within the plugin PLUMED [https://arxiv.org/abs/1310.0980 and https://arxiv.org/abs/0902.0874 and https://www.nature.com/articles/s41592-019-0506-8] using a bias factor of 25, a gaussian height of 1 kcal mol^{-1}, a gaussian sigma of 0.05 Å. Gaussian biaises were placed at a pace of 100 molecular dynamics time steps. The metadynamics have been performed during 5 ns.

Regeneration of PFOA: The experiments were carried out in 75 mL beaker containing 50 mL of DI water with 40 mg of 3D-PSHΔ. The beakers were capped with Parafilm to reduce the evaporation. The 3D-PSHΔ was stirred during 24 h and the samples were analyzed using LC-MS. For desorption, the 3D-PSHΔ was added to a mixture of ethanol/deionized water and stirred for 24 h.

Sorption Kinetic of PFAS with 3D-PSHΔ and 3D-PSHΔQ^+: Solutions containing 0.5 ppm of PFOA, 0.44 ppm (0.0012 mmol L^{-1}) of PFHpA, 0.38 ppm (0.0012 mmol L^{-1}) of PFHxA, 0.32 ppm (0.0012 mmol L^{-1}) of PFPeA, 0.6 ppm (0.0012 mmol L^{-1}) of PFOS, and 0.36 ppm (0.0012 mmol L^{-1}) of PFBS were prepared.

The experiments were conducted in 75 mL beakers containing 50 mL of PFAS solution in deionized (DI) water. Kinetic studies were carried out using 3D-PSHΔ (≈45mg) and 3D-PSHΔQ^+ (≈58mg). Each experiment spanned a 24-h duration, with sampling intervals of 30 min for the initial 3 h, followed by hourly sampling until the end of the 24-h period.

Biocompatibility Test of the Molecules and the Material (3D-PSHΔ): *In vitro study on THP-1 cells*: The human monocytes cell line (THP-1) was purchased from ATCC. Cells were cultivated in RPMI 1640 + 10% fetal bovine serum + 1% penicillin/streptomycin and allowed to grow at 37 °C, under a humidified atmosphere and 5% CO2. The cytotoxicity study was performed by seeding cells into 96-well plates at 2000 cells per well in 200 µl of culture medium. One day after seeding, cells were incubated for 72 h with increasing concentrations of molecules (from 0.001 to 100 mM), and the cell survival rate after 3 days was determined by a cell death quantification assay, performed by incubating cells with Thiazolyl Blue Tetrazolium Bromide (MTT) (0.5 mg ml^{-1}) for 4 h to determine the mitochondrial enzyme activity. Then, the supernatant was removed, and 150 µl of EtOH/DMSO (1:1) was added to dissolve the MTT precipitates. Absorbance was measured at 540 nm with a microplate reader.

In vivo study on zebrafish embryos: In Vivo Toxicity in Zebrafish Embryos. Wild-type AB zebrafish strain was purchased from Zebrafish International Resource Center (ZIRC). Embryos were raised to adulthood in a circulating aquarium system inside an environmentally controlled room (28 °C, 80% humidity, 14 h light/10 h dark cycle), in the lab's facilities of Molecular mechanisms in neurodegenerative dementia (MMDN), Inserm U1198, Montpellier University, Montpellier. Fertilized embryos were collected and maintained at 28 °C. At 7 h post fertilization (hpf), embryos were examined under the microscope, and only embryos that developed normally and reached gastrula stage were selected for the study. Gastrula stage embryos were placed in a 12-well plate (6 embryos per well) and exposed to 4.5 mL of water containing or not the material (3D-PSHD) (27.75 mg). During 5 days, the development of embryos was monitored every day. Percentages of dead, chorionated, and hatched embryos were reported at different hours post fertilization (hpf): 7, 24, 48, 72, and 120 hpf. In addition, mobility, morphology, and cardiac rhythm were observed. Experiments with zebrafish embryos until 120 hpf are considered as in vitro studies according to EU Directive 2010/63/EU on the protection of animals used for scientific purposes.

Supporting Information

Supporting Information is available from the Wiley Online Library or from the author.

Acknowledgements

M.S., B.T.B., and A.C. would like to thank the French National Research Agency (ANR; PEPPISA-19-CE06-0011-01), MUSE-University of Montpellier (IMOPS), and Chimie Balard Cirimat Carnot Institute (through the ANR program N°16 CARN 0008-0) for funding this work. R.D. acknowledges CINES (project A0150914406) and TGCC (project AD010911009) for the computational resources used for simulations. M.S. and R.D. also received financial support from MITI CNRS interdisciplinary program (pollution-depollution challenge project CAPTURE). This work was also supported by the Laboratoire d'Excellence sur la Chimie des Systèmes Moléculaires et Interfaciaux (LabEx CheMISyst). The authors extend the gratitude to the zebrafish platform of the laboratory Molecular Mechanisms in Neurodegenerative Dementia (MMDN), Inserm U1198.

Conflict of Interest

The authors declare no conflict of Interest.

Data Availability Statement

The data that support the findings of this study are available from the corresponding author upon reasonable request.

Keywords

3D printing, Hydrogels, PFAS, Polymer network, Porous Sorbents, Stereolithography, Trianglamine

Received: July 23, 2024
Revised: October 25, 2024
Published online:

[1] M. G. Evich, M. J. B. Davis, J. P. McCord, B. Acrey, J. A. Awkerman, D. R. U. Knappe, A. B. Lindstrom, T. F. Speth, C. Tebes-Stevens, M. J. Strynar, Z. Wang, E. J. Weber, W. M. Henderson, J. W. Washington, *Science* **2022**, *375*, 512.
[2] R. Dhore, G. S. Murthy, *Bioresour. Technol.* **2021**, *341*, 125808.
[3] Y. Wang, S. B. Darling, J. Chen, *ACS Appl. Mater. Interfaces.* **2021**, *13*, 60789.
[4] Z. Zheng, H. Yu, W.-C. Geng, X.-Y. Hu, Y.-Y. Wang, Z. Li, Y. Wang, D.-S. Guo, *Nat. Commun.* **2019**, *10*, 5762.
[5] S. Fujii, C. Polprasert, S. Tanaka, N. P. Hong Lien, Y. Qiu, *J. Water Supply: Res. Technol.-Aqua* **2007**, *56*, 313.
[6] K. R. Miner, H. Clifford, T. Taruscio, M. Potocki, G. Solomon, M. Ritari, I. E. Napper, A. P. Gajurel, P. A. Mayewski, *Sci. Total Environ.* **2021**, *759*, 144421.
[7] A. Yang, C. Ching, M. Easler, D. E. Helbling, W. R. Dichtel, *ACS Mater. Lett.* **2020**, *2*, 1240.
[8] G. Dagorn, R. Aubert, S. Horel, L. Martinon, T. Steffen, Le Monde **2023**.
[9] Y. Wen, Á. Rentería-Gómez, G. S. Day, M. F. Smith, T.-H. Yan, R. O. K. Ozdemir, O. Gutierrez, V. K. Sharma, X. Ma, H.-C. Zhou, *J. Am. Chem. Soc.* **2022**, *144*, 11840.
[10] Z. Chen, Y.-L. Lu, L. Wang, J. Xu, J. Zhang, X. Xu, P. Cheng, S. Yang, W. Shi, *J. Am. Chem. Soc.* **2023**, *145*, 260.
[11] A. Román Santiago, S. Yin, J. Elbert, J. Lee, D. Shukla, X. Su, *J. Am. Chem. Soc.* **2023**, *145*, 9508.
[12] D. Shetty, I. Jahović, T. Skorjanc, T. S. Erkal, L. Ali, J. Raya, Z. Asfari, M. A. Olson, S. Kirmizialtin, A. O. Yazaydin, A. Trabolsi, *ACS Appl. Mater. Interfaces.* **2020**, *12*, 43160.
[13] M. J. Klemes, Y. Ling, C. Ching, C. Wu, L. Xiao, D. E. Helbling, W. R. Dichtel, *Angew. Chem.* **2019**, *131*, 12177.
[14] C. Eschauzier, E. Beerendonk, P. Scholte-Veenendaal, P. De Voogt, *Environ. Sci. Technol.* **2012**, *46*, 1708.
[15] X. Li, S. Chen, X. Quan, Y. Zhang, *Environ. Sci. Technol.* **2011**, *45*, 8498.
[16] F. Dixit, G. Munoz, M. Mirzaei, B. Barbeau, J. Liu, S. V. Duy, S. Sauvé, B. Kandasubramanian, M. Mohseni, *Environ. Sci. Technol.* **2022**, *56*, 6212.
[17] X. Lei, Q. Lian, X. Zhang, T. Wang, M. Gee, W. Holmes, S. Jin, S. K. Ponnusamy, D. D. Gang, M. E. Zappi, *Chemosphere* **2022**, *308*, 136379.

[18] X. Tan, P. Dewapriya, P. Prasad, Y. Chang, X. Huang, Y. Wang, X. Gong, T. E. Hopkins, C. Fu, K. V. Thomas, H. Peng, A. K. Whittaker, C. Zhang, *Angew. Chem. Int. Ed.* **2022**, *61*, 202213071.
[19] F. Dixit, R. Dutta, B. Barbeau, P. Berube, M. Mohseni, *Chemosphere* **2021**, *272*, 129777.
[20] C. Gomri, B. T. Benkhaled, A. Chaix, C. Dorandeu, J. Chopineau, E. Petit, K. Aissou, D. Cot, M. Cretin, M. Semsarilar, *Carbohydr. Polym.* **2023**, *319*, 121189.
[21] R. Li, S. Alomari, R. Stanton, M. C. Wasson, T. Islamoglu, O. K. Farha, T. M. Holsen, S. M. Thagard, D. J. Trivedi, M. Wriedt, *Chem. Mater.* **2021**, *33*, 3276.
[22] R. Li, N. N. Adarsh, H. Lu, M. Wriedt, *Matter* **2022**, *5*, 3161.
[23] W. Ji, L. Xiao, Y. Ling, C. Ching, M. Matsumoto, R. P. Bisbey, D. E. Helbling, W. R. Dichtel, *J. Am. Chem. Soc.* **2018**, *140*, 12677.
[24] H. Li, A. L. Junker, J. Wen, L. Ahrens, M. Sillanpää, J. Tian, F. Cui, L. Vergeynst, Z. Wei, *Chem. Eng. J.* **2023**, *452*, 139202.
[25] L. Xiao, Y. Ling, A. Alsbaiee, C. Li, D. E. Helbling, W. R. Dichtel, *J. Am. Chem. Soc.* **2017**, *139*, 7689.
[26] X. Liu, C. Zhu, J. Yin, J. Li, Z. Zhang, J. Li, F. Shui, Z. You, Z. Shi, B. Li, X.-H. Bu, A. Nafady, S. Ma, *Nat. Commun.* **2022**, *13*, 2132.
[27] N. A. Lundquist, M. J. Sweetman, K. R. Scroggie, M. J. H. Worthington, L. J. Esdaile, S. F. K. Alboaiji, S. E. Plush, J. D. Hayball, J. M. Chalker, *ACS Sustainable Chem. Eng.* **2019**, *7*, 11044.
[28] W. A. Freeman, W. L. Mock, N. Y. Shih, *J. Am. Chem. Soc.* **1981**, *103*, 7367.
[29] K. Kim, N. Selvapalam, Y. H. Ko, K. M. Park, D. Kim, J. Kim, *Chem. Soc. Rev.* **2007**, *36*, 267.
[30] S. Shinoda, *Chem. Soc. Rev.* **2013**, *42*, 1825.
[31] D.-S. Guo, Y. Liu, *Chem. Soc. Rev.* **2012**, *41*, 5907.
[32] T. Ogoshi, S. Kanai, S. Fujinami, T. Yamagishi, Y. Nakamoto, *J. Am. Chem. Soc.* **2008**, *130*, 5022.
[33] P. Della Sala, R. Del Regno, C. Talotta, A. Capobianco, N. Hickey, S. Geremia, M. De Rosa, A. Spinella, A. Soriente, P. Neri, C. Gaeta, *J. Am. Chem. Soc.* **2020**, *142*, 1752.
[34] J. Gawronski, K. Gawronska, J. Grajewski, M. Kwit, A. Plutecka, U. Rychlewska, *Chem. A Eur. J.* **2006**, *12*, 1807.
[35] A. Chaix, G. Mouchaham, A. Shkurenko, P. Hoang, B. Moosa, P. M. Bhatt, K. Adil, K. N. Salama, M. Eddaoudi, N. M. Khashab, *J. Am. Chem. Soc.* **2018**, *140*, 14571.
[36] K. N. Chappanda, A. Chaix, S. G. Surya, B. A. Moosa, N. M. Khashab, K. N. Salama, *Sens. Actuators, B* **2019**, *294*, 40.
[37] T. Huang, B. A. Moosa, P. Hoang, J. Liu, S. Chisca, G. Zhang, M. AlYami, N. M. Khashab, S. P. Nunes, *Nat. Commun.* **2020**, *11*, 5882.
[38] B. T. Benkhaled, A. Chaix, C. Gomri, S. Buys, N. Namar, N. Sehoulia, R. Jadhav, J. Richard, L. Lichon, C. Nguyen, M. Gary-Bobo, M. Semsarilar, *ACS Appl. Mater. Interfaces.* **2023**, *15*, 42942.
[39] A. Dey, S. Chand, L. O. Alimi, M. Ghosh, L. Cavallo, N. M. Khashab, *J. Am. Chem. Soc.* **2020**, *142*, 15823.
[40] A. Dey, S. Chand, M. Ghosh, M. Altamimy, B. Maity, P. M. Bhatt, I. A. Bhat, L. Cavallo, M. Eddaoudi, N. M. Khashab, *Chem. Commun.* **2021**, *57*, 9124.
[41] A. Dey, S. Chand, B. Maity, P. M. Bhatt, M. Ghosh, L. Cavallo, M. Eddaoudi, N. M. Khashab, *J. Am. Chem. Soc.* **2021**, *143*, 4090.
[42] Y. Ding, A. Dey, L. O. Alimi, P. M. Bhatt, J. Du, C. Maaliki, M. Eddaoudi, J. Jacquemin, N. M. Khashab, *Chem. Mater.* **2022**, *34*, 197.
[43] Y. Ding, L. O. Alimi, J. Du, B. Hua, A. Dey, P. Yu, N. M. Khashab, *Chem. Sci.* **2022**, *13*, 3244.
[44] X. Liu, L. O. Alimi, N. M. Khashab, *Chem. Commun.* **2022**, *58*, 9369.
[45] B. Hua, L. O. Alimi, G. Zhang, Y. Ding, B. Moosa, W. S. Baslyman, N. M. Khashab, *Mater. Today Chem.* **2022**, *24*, 100840.
[46] X. Zhu, G. Zhang, L. O. Alimi, B. M. Moosa, A.-H. Emwas, F. Fang, N. M. Khashab, *Chem. Mater.* **2023**, *35*, 9160.
[47] I. M. Andrei, A. Chaix, B. T. Benkhaled, R. Dupuis, C. Gomri, E. Petit, M. Polentarutti, A. Van Der Lee, M. Semsarilar, M. Barboiu, *J. Am. Chem. Soc.* **2023**, *145*, 21213.
[48] W. Xu, G. Li, H. Qu, C. Ma, H. Zhang, J. Cheng, H. Li, *ACS Nano* **2023**, *17*, 19305.
[49] V. Van Tran, D. Park, Y.-C. Lee, *Environ. Sci. Pollut. Res.* **2018**, *25*, 24569.
[50] R. Ganesamoorthy, V. K. Vadivel, R. Kumar, O. S. Kushwaha, H. Mamane, *J. Cleaner Prod.* **2021**, *329*, 129713.
[51] R. Gusain, N. Kumar, S. S. Ray, *Coord. Chem. Rev.* **2020**, *405*, 213111.
[52] R. Gusain, N. Kumar, S. S. Ray, *ChemistrySelect* **2023**, *8*, 202300738.
[53] J. Shojaeiarani, A. Shirzadifar, D. S. Bajwa, *Microporous Mesoporous Mater.* **2021**, *327*, 111382.
[54] G. A. Appuhamillage, D. R. Berry, C. E. Benjamin, M. A. Luzuriaga, J. C. Reagan, J. J. Gassensmith, R. A. Smaldone, *Polym. Int.* **2019**, *68*, 964.
[55] A. Masud, C. Zhou, N. Aich, *Environ. Sci.: Nano* **2021**, *8*, 399.
[56] Y. Miao, W. Peng, W. Wang, Y. Cao, H. Li, L. Chang, Y. Huang, G. Fan, H. Yi, Y. Zhao, T. Zhang, *Sep. Purif. Technol.* **2022**, *283*, 120176.
[57] E. Baigorria, S. Souza Dos Santos, M. R. De Moura, L. F. Fraceto, *Mater. Today Chem.* **2023**, *30*, 101559.
[58] R. Pei, L. Fan, F. Zhao, J. Xiao, Y. Yang, A. Lai, S.-F. Zhou, G. Zhan, *J. Hazard. Mater.* **2020**, *384*, 121418.
[59] J. Gawroński, H. Kołbon, M. Kwit, A. Katrusiak, *J. Org. Chem.* **2000**, *65*, 5768.
[60] S. B. G. Blanquer, M. Werner, M. Hannula, S. Sharifi, G. P. R. Lajoinie, D. Eglin, J. Hyttinen, A. A. Poot, D. W. Grijpma, *Biofabrication* **2017**, *9*, 025001.
[61] J. Yu, L. Lv, P. Lan, S. Zhang, B. Pan, W. Zhang, *J. Hazard. Mater.* **2012**, *225*, 99.
[62] H. Wan, R. Mills, K. Qu, J. C. Hower, M. Abdul Mottaleb, D. Bhattacharyya, Z. Xu, *Chem. Eng. J.* **2022**, *433*, 133271.
[63] A. Maimaiti, S. Deng, P. Meng, W. Wang, B. Wang, J. Huang, Y. Wang, G. Yu, *Chem. Eng. J.* **2018**, *348*, 494.
[64] C. Mejías, J. Martín, J. Luis Santos, I. Aparicio, E. Alonso, *Environ. Res.* **2023**, *216*, 114834.
[65] Y. Yuan, L. Feng, X. He, X. Liu, N. Xie, Z. Ai, L. Zhang, J. Gong, *J. Hazard. Mater.* **2022**, *423*, 127176.
[66] X. Gao, J. Chorover, *Environ. Chem.* **2012**, *9*, 148.
[67] A. Laio, F. L. Gervasio, *Rep. Prog. Phys.* **2008**, *71*, 126601.
[68] R. Dupuis, J. S. Dolado, J. Surga, A. Ayuela, *ACS Sustainable Chem. Eng.* **2018**, *6*, 15015.
[69] A. C. T. Van Duin, S. Dasgupta, F. Lorant, W. A. Goddard, *J. Phys. Chem. A.* **2001**, *105*, 9396.
[70] S. K. Singh, S. G. Srinivasan, M. Neek-Amal, S. Costamagna, A. C. T. Van Duin, F. M. Peeters, *Phys. Rev. B.* **2013**, *87*, 104114.
[71] Y. Liu, J. Hu, H. Hou, B. Wang, *Chem. Phys.* **2020**, *538*, 110888.
[72] P.-J. Huang, M. Hwangbo, Z. Chen, Y. Liu, J. Kameoka, K.-H. Chu, *ACS Omega* **2018**, *3*, 17447.
[73] C. Xu, H. Chen, F. Jiang, *Colloids Surf. A* **2015**, *479*, 60.
[74] S. Deng, Y. Q. Zheng, F. J. Xu, B. Wang, J. Huang, G. Yu, *Chem. Eng. J.* **2012**, *193–194*, 154.